Cement and Concrete Research 175 (2024) 107367

Contents lists available at ScienceDirect

Cement and Concrete Research

journal homepage: www.elsevier.com/locate/cemconres

Chemical structure and complex growth modes of magnesium silicate hydrate: Nanoparticle orientation, aggregation, and fusion

Dylan Singh [a,b], Trinh Thao My Nguyen [a,c,d], Evann Bustamantes [a,b,e], Abdul Wahab [a,b], Ahmad Hamzah Yousaf [a,b,e], Ian Shortt [a,b], Frank W. Foss Jr [d], Maria Konsta-Gdoutos [b,f], Sang Soo Lee [g], Erika La Plante [a,b,c,*]

[a] Department of Materials Science and Engineering, University of Texas at Arlington, Arlington, TX 76019, United States of America
[b] Center for Advanced Construction Materials, University of Texas at Arlington, Arlington, TX 76019, United States of America
[c] Department of Materials Science and Engineering, University of California, Davis, Davis, CA 95616, United States of America
[d] Department of Chemistry and Biochemistry, University of Texas at Arlington, Arlington, TX 76019, United States of America
[e] Department of Mechanical and Aerospace Engineering, University of Texas at Arlington, Arlington, TX 76019, United States of America
[f] Department of Civil Engineering, University of Texas at Arlington, Arlington, TX 76019, United States of America
[g] Chemical Sciences and Engineering Division, Argonne National Laboratory, Lemont, IL 60439, United States of America

ARTICLE INFO

Keywords:
Non-classical crystallization
Fourier-transform infrared spectroscopy
Atomic force microscopy
Particle attachment
Hierarchical structures

ABSTRACT

The extent of utilization of magnesium silicate hydrate (MSH) in construction is limited partly because of insufficient data ascertaining the kinetics of its precipitation. Here, MSH grown homogeneously or heterogeneously in the range of magnesium to silicon solution molar concentration ratios, [Mg]/[Si] = 0.5–1.5, and temperature = 25–80 °C was analyzed for its chemical structure and morphology. Infrared spectroscopy and geochemical modeling show that increasing the [Mg]/[Si] ratio results in less silicate polymerization in MSH. Atomic force microscopy reveals the presence of nanoparticles that aggregate and fuse to form films. Oriented attachment of nanoparticles and features indicative of enhanced crystallinity were observed at higher temperatures and longer reaction times. These data provide direct evidence for the persistence of hierarchical structures (i.e., nanoparticles forming 3D microparticles and 2D film layers) at the nanoscale to mesoscale. These findings offer insights into the precise chemical synthesis of MSH and its widespread use as a binder for construction purposes.

1. Introduction

Increasing environmental concerns arising from concrete's high energy consumption and carbon dioxide (CO_2) footprint have prompted a growing interest in strategies to improve concrete durability, partially replace ordinary Portland cement (OPC), or create new binder chemistries [1–4]. However, knowledge generation in the cement industry is often driven by demands for specific functions and requires extensive experimental designs based on trial and error [5]. Key challenges that preclude widespread implementation of alternative cementitious materials include: (1) the need for scarce or energy-intensive reactants, while substitutes based on abundant magnesium-based precursors are relatively less explored [6], (2) the limited understanding of the thermodynamic and kinetic controls on the formation of nanoscale and mesoscale structures leading to porosity filling in hydraulic cements [7], and (3) the inadequate understanding of the structure–property relationships in cementitious systems at the nanoscale and beyond. This lack of knowledge impedes the tailored synthesis of binders with predictable properties.

Calcium silicate hydrate (CSH) that makes up OPC-based concrete has a structure akin to defected tobermorite ($Ca_5H_2Si_6O_{18}{\cdot}8H_2O$) or jennite ($Ca_9H_2Si_6O_{18}(OH)_8{\cdot}6H_2O$) [8–12], wherein Ca–O chains are sandwiched by paired and bridging silicate tetrahedra, and water molecules occupy the interlayers. In contrast, magnesium and silicon-based cements, as in magnesium silicate hydrate (MSH), are less explored [6]. MSH is attractive not only as a cementitious infrastructure material but also for special applications. For instance, the higher acidity of MSH cements compared to CSH cements reduces the persistence of an alkaline plume that results in the degradation of the surrounding clay in nuclear waste repositories [13]. Low-pH cements can also be used for

* Corresponding author.
E-mail address: eclaplante@ucdavis.edu (E. La Plante).

https://doi.org/10.1016/j.cemconres.2023.107367
Received 1 February 2023; Received in revised form 19 October 2023; Accepted 29 October 2023
Available online 8 November 2023

Table 1
Description of conditions for **Set A** experiments. [Mg] and [Si] are initial solution parameters obtained based on the measured masses of precursors and the volume of the growth solution. The same Mg and Si concentrations are used in the models. The saturation indices are calculated based on the measured pH (i.e., the modeled pH is equal to the measured pH). In the simulations, the measured pH is attained by adding CO_2 (see Tables S1–S4). Positive values of saturation index indicate thermodynamic favorability for the formation of the phase.

[Mg] (mM)	[Si] (mM)	[Mg]/[Si] (M/M)	pH (meas.)	Time (h)	T (°C)	SI $M_{0.75}SH$	SI $M_{1.5}SH$	SI Brucite	SI $SiO_{2\ (am)}$
101	200	0.505	12.57	480	25	8.94	8.43	4.25	−1.95
111	200	0.555	12.50	480	25	9.02	8.46	4.24	−1.89
121	200	0.605	12.42	480	25	9.12	8.48	4.20	−1.82
130	200	0.650	12.34	480	25	9.20	8.49	4.16	−1.75
139	200	0.695	12.25	480	25	9.28	8.49	4.11	−1.67
151	200	0.755	11.93	480	25	9.48	8.39	3.84	−1.37
160	200	0.800	11.79	480	25	9.57	8.35	3.73	−1.25
169	200	0.845	11.47	480	25	9.73	8.21	3.43	−0.94
179	200	0.895	10.70	480	25	9.98	7.66	2.53	−0.14
191	200	0.955	10.23	480	25	9.95	7.15	1.87	0.34
201	200	1.005	9.95	480	25	9.85	6.77	1.44	0.62
212	200	1.060	9.79	480	25	9.79	6.55	1.18	0.78
224	200	1.120	9.68	480	25	9.74	6.40	1.02	0.88
230	200	1.150	9.63	480	25	9.72	6.33	0.94	0.93
240	200	1.200	9.58	480	25	9.71	6.28	0.87	0.97
256	200	1.280	9.48	480	25	9.66	6.14	0.72	1.06
261	200	1.305	9.51	480	25	9.70	6.21	0.79	1.03
272	200	1.360	9.52	480	25	9.74	6.26	0.84	1.01
278	200	1.390	9.48	480	25	9.72	6.21	0.77	1.05
290	200	1.450	9.46	480	25	9.73	6.20	0.76	1.06
300	200	1.500	9.46	480	25	9.75	6.23	0.78	1.06

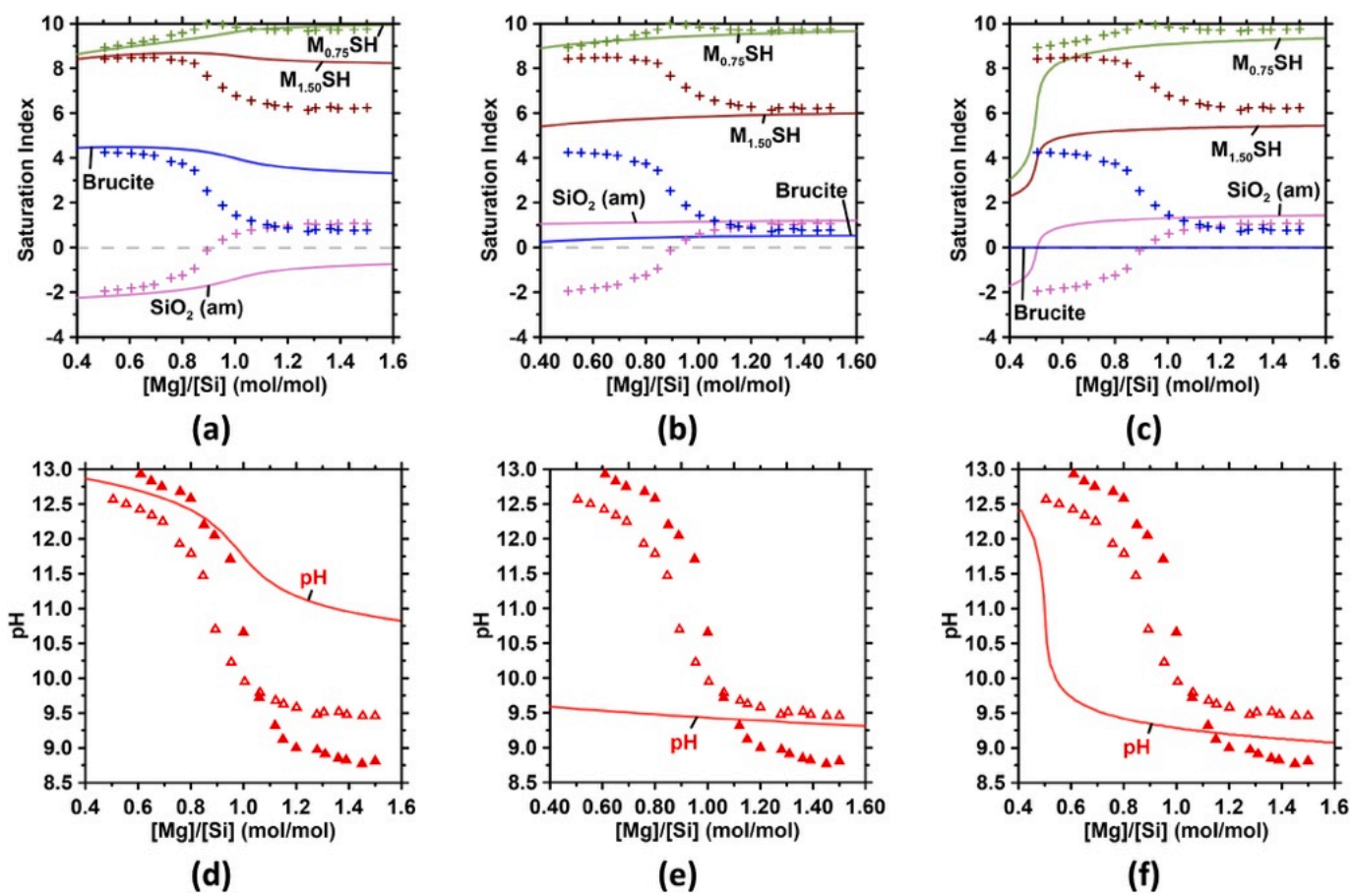

Fig. 1. (a–c) Saturation index and (d–f) pH of growth solutions for Set A experiments (see Tables 1, S2, S3, and S4) as a function of [Mg]/[Si] at 25 °C. The calculations were performed using PHREEQC [44] with the Cemdata18 database [45] for: (a), (d) as-mixed (within 2 min) solutions, (b), (e) the solutions equilibrated with atmospheric CO_2 (420 ppm), and (c), (f) the solutions equilibrated with brucite (i.e., $SI_{brucite} = 0$), represented as solid lines. The measured pH values and corresponding saturation indices are given in symbols (*open red triangles*: initial pH; *solid red triangles*: pH after 11 days of reaction; *crosses*: saturation indices). Dashed gray lines mark a saturation index of 0, which indicates dissolution/precipitation equilibrium. (For interpretation of the references to color in this figure legend, the reader is referred to the web version of this article.)

Table 2
FTIR wavenumbers and putative species detected in the sample.

Species	Characteristic	Wavenumber (cm^{-1})	Reference
Q^1_b	Bending	622, 634	[38,39]
Q^1_s	Stretching	835	[38,39]
Q^2	Bending	902, 908	[38,39]
Q^3	Stretching	977, 985	[38,39]
Si—O^-	Stretching	1350–1397	[59]
H_2O	Bending	1637	[38,39,59]
O—H	Stretching	3383	[38,39]
MgO—H	Stretching	3676	[38,39]

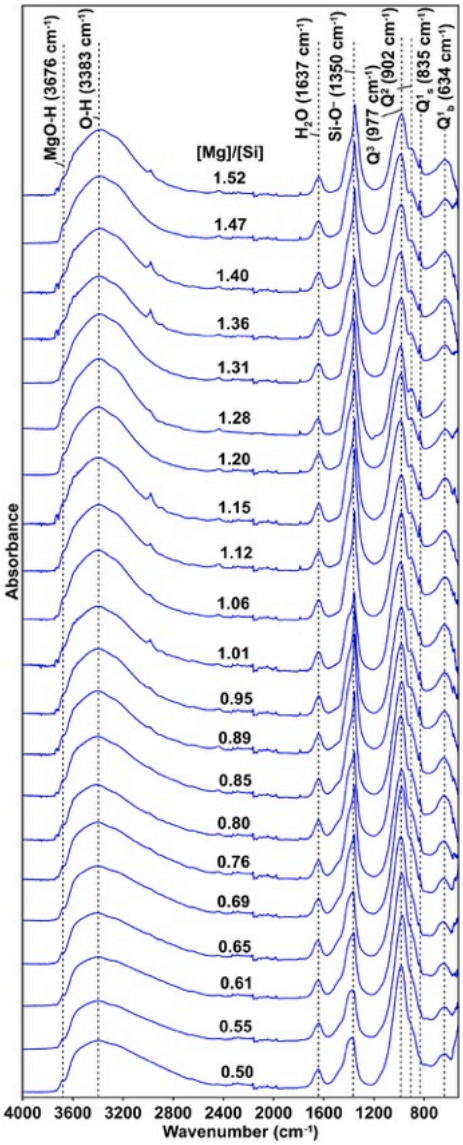

Fig. 2. Fourier-transform infrared spectra of MSH samples synthesized from growth solutions with [Mg]/[Si] molar ratios ranging from 0.50 to 1.52 (**Set A**, Table 1). The spectra are labeled using their respective solution [Mg]/[Si] molar ratios. The wavenumbers corresponding to the species detected in each sample are labeled by dashed vertical lines.

stabilization of CO_2 injection wells during enhanced oil recovery or in situ geologic CO_2 sequestration, which requires cements that are stable under CO_2-rich conditions [14]. Furthermore, interest in MSH has been motivated by its potential use for immobilization of heavy metals by surface sorption or precipitation of metal-containing cementitious phases that have reduced solubility and hazardousness compared to the metal pollutants [6,15–19]. Finally, MSH finds use in catalysis owing to the tunable acidity of its surface groups and the high defective site density in the talc-like structure [20].

MSH can be synthesized from widely abundant magnesium-rich silicate solids and brines [6,21–25]. In nature, MSH analogs are found in ultramafic rock formations that are characterized by serpentinization [26–28]. Crystalline MSH has also been observed in a concrete sea-wall, presumably arising from the breakdown of CSH and phase alterations induced by the Mg-rich seawater [29]. The dissimilarity between Ca^{2+} and Mg^{2+} ions [30,31] may lead to distinct chemical properties of CSH and MSH. Nonetheless, both phases are composed of silicate tetrahedra that polymerize to form double chains or sheets that are poorly crystalline and highly defective. Both solids also feature negative surface charges arising from the silanol (Si—O—H) groups that deprotonate to greater extents as pH increases, with Ca^{2+} or Mg^{2+} compensating for the generation of silicate charges [32–34].

Insights into MSH synthesis can be gained from studies on Mg-rich phyllosilicates [35]. Talc ($Mg_3(Si_4O_{10})(OH)_2$) and serpentine ($Mg_3(Si_2O_5)(OH)_4$) have been observed to form days to weeks after reaction of magnesia and silica at high temperatures and pressures (75–135 °C, ~138 MPa), with MSH gels either co-precipitating or forming as intermediate phases [36,37]. MSH has been batch synthesized from aqueous solutions by reacting MgO with silica fume, or by mixing stoichiometric amounts of magnesium nitrate and sodium silicate in water (as employed in this study), revealing poorly ordered agglomerates with typical Mg/Si molar ratios of 0.6–1.2, depending on the reaction time and temperature [33,38–41]. In another series of studies, X-ray spectroscopy and ab initio calculations reveal that MSH synthesized for 1–12 months with molar Mg/Si = 0.7–1.5 have a talc-like TOT (tetrahedral-octahedral-tetrahedral) structure (Mg/Si = 0.75) at low Mg/Si and a serpentine-like TO structure (Mg/Si = 1.5) at high Mg/Si, in which a high defect density in the silica layers is associated with an increase in the Mg/Si molar ratio [33,39,40,42,43].

The use of MSH in construction applications is limited, in part because of the insufficient data ascertaining its "*cementitious character*", i.e., rates of precipitation, structural mechanisms for strengthening, and stability in relevant environments. Phase assemblages, structures, morphologies, and growth modes of MSH inform these aspects. Therefore, in this study, we examine the morphology and chemical structures of MSH using high-resolution atomic force microscopy (AFM) and Fourier-transform infrared spectroscopy (FTIR), supplemented by geochemical modeling. Investigations of MSH structures at high spatial and temporal resolutions will enable a mechanistic understanding of the properties of MSH-based structural and functional materials, and the manipulation of these properties. In addition, the knowledge acquired from this study can be extended to less-studied magnesium-based cements (e.g., magnesium carbonate) and to analogous systems such as CSH. Our ultimate goal is to identify precise chemical pathways for MSH synthesis and contribute to the knowledge of processing–structure–property relationships in MSH, thus establishing its viability as a binder material for construction purposes and an alternative to OPC.

2. Materials and methods

2.1. Sample preparation

Two sets of samples that separately address chemical structure and growth morphology were prepared. One set of samples (**Set A**) was prepared by mixing stock solutions of sodium metasilicate pentahydrate ($Na_2SiO_3{\cdot}5H_2O$, 99 % purity, 214.14 g/mol) and magnesium nitrate hexahydrate ($Mg(NO_3)_2{\cdot}6H_2O$, ≥95 % purity, 256.41 g/mol) in a polypropylene centrifuge tube to generate 30 mL growth solutions (i.e., solutions that induce the growth of MSH) with final concentrations of [Mg] = 100–300 mM and [Si] = 200 mM, where the brackets, [ ], indicate the total concentration of the element in the solution. Ultrapure deionized (DI) water (ThermoFisher Scientific Barnstead MicroPure,

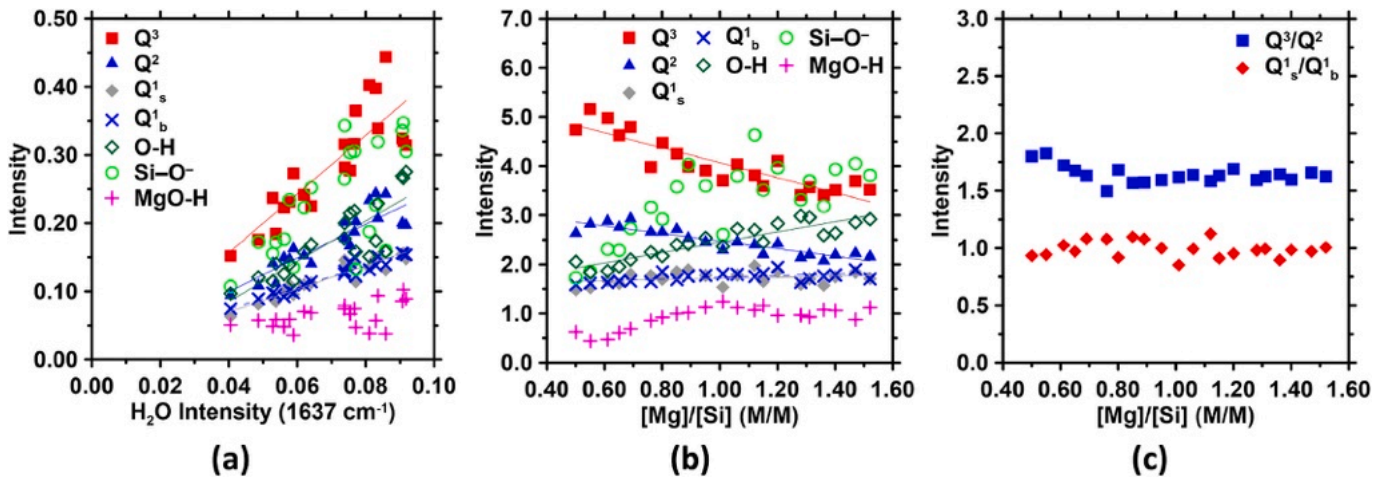

Fig. 3. (a) Absorbance intensity for various species as a function of absorbance intensity of the H_2O peak. (b) H_2O-normalized absorbance intensity as a function of [Mg]/[Si]. (c) Q^3/Q^2 and Q^1_s/Q^1_b absorbance ratios as a function of [Mg]/[Si].

≥18.20 MΩ·cm) was used for preparation of solutions. The centrifuge tubes were sealed and stored at ambient temperature (25 ± 2 °C) for 20 days, and then centrifuged and decanted to separate the solid precipitates from the residual solution. Then, the precipitates were left to dry in the centrifuge tube covered loosely with a Kimwipe™ at ambient temperature and pressure for 1–3 weeks. The pH values of the growth solutions were measured within ~2 min of solution preparation ("initial pH") and after 11 days of reaction using a multiparameter benchtop meter (ThermoFisher Scientific Orion™ VersaStar Pro™) calibrated over pH = 7–12. Another set of samples (**Set B**) was prepared by reacting a growth solution with single crystal surfaces, i.e., either synthetic MgO (100) (~3–10 mm in length and width and ~0.5 mm in height) (SPI Supplies) or muscovite mica (001) (10 mm in diameter, 0.21 mm thick, Grade V1, Ted Pella). Immediately after cleaving (within a few seconds), the crystal substrates were exposed briefly to ultra-high purity (UHP) N_2 gas to remove any surface debris. Growth solutions were prepared either by adding $Na_2SiO_3{\cdot}5H_2O$ salt in DI water (i.e., undersaturated solutions) or by mixing $Mg(NO_3)_2{\cdot}6H_2O$, $Na_2SiO_3{\cdot}5H_2O$, and DI water (i.e., supersaturated solutions). The reaction temperature was maintained using a heating plate (Tables 1 and 3). At the end of each experiment, the single crystal was wicked on its edge using a Kimwipe™ and then exposed briefly to UHP N_2 gas to blow off any excess liquid. The samples were stored in a loosely covered (with a Kimwipe™) polyethylene container at ambient temperature and pressure conditions prior to characterization. For both **Set A** and **Set B** samples, the precipitates were not washed to minimize any potential alteration after removal of the residual solution. The solution speciation and saturation states were calculated using PHREEQC [44] with the Cemdata18 database, which contains thermodynamic data for various phases that typically occur in cementitious systems, including $M_{0.75}SH$, $M_{1.5}SH$, brucite, and amorphous silica [45]. The geochemical models explicitly account for the pH-dependent speciation of the elements as well as their complexation with other species, through mass action equations. The pH values of the stock solutions closely match the calculated pH, suggesting complete dissolution of sodium metasilicate and magnesium nitrate in the stock solutions. The saturation index (SI) is defined as log Ω, where the saturation ratio, $\Omega = Q/K_{sp}$, Q is the ion activity product, and K_{sp} is the solubility product of a given phase. The residual sum of squares, $RSS = \sum_{i=1}^{n}\left(y_i - f(x_i)\right)^2$, where y_i is the ith value of the variable to be predicted and $f(x_i)$ is the predicted value of y_i from the geochemical model, is used to quantify the discrepancy between the measured data and the geochemical model.

2.2. Characterization of MSH precipitates

To characterize the molecular structure of the precipitates, infrared absorbance measurements were performed using a Nicolet iS50 (Thermo Scientific) FTIR spectrometer with an attenuated total reflectance (ATR) attachment and a deuterated triglycine sulfate (DTGS) KBr detector. Infrared spectra were collected using the following parameters: 32 background and sample scans, atmospheric suppression option, and a wavenumber range of 525–4000 cm^{-1}. Selected samples were analyzed using scanning electron microscopy with energy dispersive spectroscopy (SEM-EDS) (Hitachi S-3000N Variable Pressure SEM) with a working distance of 15 mm and an accelerating voltage of 25 kV. Samples were ground and coated with Au/Pt for 2 min using the Hummer VI sputtering system prior to SEM imaging. X-ray diffraction (XRD) data were obtained using a Siemens D-500 X-ray diffractometer in a θ-2θ configuration for thin films deposited on the MgO substrate. A Cu Kα incident beam with the wavelength of 1.54059 Å was used, and a scan range of 3–5° to 60° 2θ, step size of 0.02°, dwell time of 0.5–1 s, and a working voltage and current of 40 kV and 30 mA were employed. The diffractograms reflect the sum of intensities for three repeated measurements for each sample. Ambient imaging of MSH grown on single crystal substrates was conducted using a Cypher ES AFM (Oxford Instruments Asylum Research) equipped with a heating and cooling sample stage (0–120 °C) with a perfluoroelastomer (FFKM) seal. Imaging was carried out in tapping mode (AC mode) to reduce shear forces on the precipitates associated with tip movement [46]. A monolithic silicon probe featuring a rectangular cantilever with a 70 nm thick gold coating on the detector side and the following characteristics (nominal values are indicated in parentheses): force constant (3 N/m), resonance frequency (75 kHz), length (225 μm), width (28 μm), and thickness (3 μm), shape (rotated), height (17 μm), setback (15 μm), radius (<10 nm), half cone angle (20°–25° along cantilever axis, 25°–30° from side, 10° at the apex), was used.

3. Results and discussion

This study describes the growth kinetics of MSH. Section 3.1 presents detailed chemical characterization of bulk MSH precipitates using FTIR, and Section 3.2 presents growth modes and morphology of substrate-precipitated MSH observed using AFM. The inhomogeneity of the samples and the large contribution of MgO/mica substrate to the signal preclude quantitative interpretation of the FTIR data for the **Set B** samples. Likewise, the large roughness of the **Set A** samples precludes their detailed morphological evaluation, i.e., measurements of sub-nm heights and lateral dimensions using AFM. Taken together, these

Table 3
Description of conditions for **Set B** experiments. [Mg] and [Si] are initial solution parameters obtained based on the measured masses of precursors and the volume of the growth solution. The saturation indices are calculated based on the initial solution composition at the given experimental temperature. Positive values of saturation index indicate thermodynamic favorability for the formation of the phase.

Type	Substrate	[Mg] (mM)	[Si] (mM)	[Mg]/[Si] (M/M)	pH (meas.)	pH (calc.)	Time (h)	T (°C)	V (mL)	SI $M_{0.75}SH$	SI $M_{1.50}SH$	SI $Mg(OH)_2$	SI SiO_2 (am)
Ex situ	MgO	0	200	0	12.52	11.77	4	80	0.5	–	–	–	−3.02
Ex situ	MgO	0	200	0	12.52	11.77	72	80	0.5	–	–	–	−3.02
Ex situ	MgO	50	100	0.5	11.94	12.52	2	~25	2	8.52	7.95	3.89	−1.89
Ex situ	MgO	100	100	1.0	10.18	11.61	2	~25	2	9.19	8.08	3.62	−1.35
Ex situ	MgO	150	100	1.5	9.73	10.92	2	~25	2	9.43	7.86	3.16	−0.88
Ex situ	Mica	200	200	1.0	10.33	11.74	2	~25	2	9.61	8.57	3.99	−1.41
In situ	MgO	0	10.2	0	12.05	11.93	2	25	0.025	–	–	–	−1.50
In situ[b]	MgO	0	200	0	12.98	12.66	15	40	0.025	–	–	–	−2.59
In situ[b]	MgO	0	200	0	12.96	12.93	20	30	0.025	–	–	–	−2.48
In situ[a]	MgO	0	200	0	12.96	12.41	5	50	0.025	–	–	–	−2.69
In situ[b]	MgO	0	200	0	12.96	12.18	8	60	0.025	–	–	–	−2.80
In situ	MgO	5	100.2	0.05	12.57	12.64	7	30	0.025	6.92	6.56	3.10	−2.14
In situ[a]	MgO	10	10	1	10.29	11.22	3	25	0.025	7.55	6.48	2.58	−1.39
In situ	MgO	15	10.2	1.5	9.90	10.94	20	25	0.025	6.48	7.68	2.49	−1.26
In situ	MgO	37.4	54.5	0.7	11.67	12.11	8	25	0.025	8.48	7.60	3.44	−1.57
In situ[b]	Mica	100	100	1	10.18	11.61	4	25	0.025	9.19	8.08	3.62	−1.35
In situ	Mica	200	200	1	10.33	11.74	2	25	0.025	9.61	8.57	3.99	−1.41

[a] $n = 3$.
[b] $n = 2$.

complementary data reveal the complex growth modes and structure of MSH.

3.1. *The molecular structure of homogeneously grown MSH and associated phases*

3.1.1. *Geochemical modeling*

The conditions for homogeneous synthesis experiments (**Set A**) are shown in Table 1. Geochemical modeling shows that the reaction solutions are supersaturated with respect to $M_{0.75}SH$, $M_{1.50}SH$, and brucite ($Mg(OH)_2$), and undersaturated with respect to amorphous silica (SiO_2 (am)) (Fig. 1a). The measured and calculated pH values match reasonably well at low [Mg]/[Si] (≤0.9) and higher pH (Fig. 1d) (RSS = 4.0) but they deviate from each other at high [Mg]/[Si] (>0.9) and lower pH (Fig. 1d). We speculate that this difference results from two factors: (1) equilibration with atmospheric CO_2 (Fig. 1e) (RSS = 1.31) and (2) precipitation of brucite (Fig. 1f) (RSS = 2.85). Both scenarios can result in a pH decrease, leading to undersaturation with respect to $M_{0.75}SH$ and $M_{1.50}SH$ and supersaturation with respect to SiO_2 (am). Fig. 1e shows that the modeled pH values do not match measured pH values at lower [Mg]/[Si], where the pH values are higher and the solution is more susceptible to carbonation. This observation suggests that the discrepancies between the measured and calculated pH are caused not by carbonation (Fig. 1b, e) but by the rapid (within seconds) precipitation of brucite at high [Mg]/[Si] (>0.9) (Fig. 1c, f). These compositional changes likely occurred rapidly, prior to the measurement of pH, i.e., <2 min after solution preparation. Although geochemical modeling indicates that the degree of supersaturation with respect to brucite *decreases* (thus resulting in *less* precipitation) with increasing [Mg]/[Si] that corresponds with decreasing pH (Table 1), the similarity of the measured pH to that calculated if brucite precipitates (Fig. 1c) suggest increased brucite precipitation at high [Mg]/[Si], consistent with the observations in a prior work [39]. This implies a kinetic control on brucite precipitation. Specifically, at lower [Mg]/[Si] (i.e., higher [Si] relative to [Mg]), the formation of MSH is favored over brucite, sequestering Mg^{2+} ions in solution and consequently inhibiting brucite formation. Notably, the initial rapid precipitation of MSH at high [Mg]/[Si] will also result in a decrease in pH.

Geochemical modeling also shows that in neutral to moderately alkaline pH (<9.5) conditions, the aqueous complexation of Mg with Si and OH is minor, and >99 % of total dissolved Mg occurs as Mg^{2+}. The extent of complexation of Mg^{2+} with OH^- to form $MgOH^+$ species increases with increasing pH, e.g., ~93 % at pH 10.5 and 50 % at pH 11.6, consistent with previous analysis [33]. Dissolved Mg^{2+} ions are strongly hydrated by six water molecules forming the $[Mg(H_2O)_6]^{2+}$ species [47–49]. Thus, precipitation reactions in the Mg–Si–H_2O system involve silica polymerization and ligand exchange around highly stable magnesium–water complexes to an extent that depends on the size, charge, rigidity, polarizability, and electron density distribution of the ligand (herein, water) [50,51].

3.1.2. *Evolution of chemical structure as a function of Mg/Si molar ratio*

Adjusting the molar ratio of the solutions affects the saturation state as shown above (Table 1, Fig. 1). To reveal the nature of the phases that form, we collected infrared absorbance spectra of the **Set A** precipitates (Table 2, Fig. 2). The FTIR spectra for samples synthesized under [Mg]/[Si] ratios between 0.50 and 1.52 are presented, showing the similarity in the nature of the various species detected (Fig. 2). It has been shown that for long reaction times (i.e., one year), MSH's Mg/Si molar ratio reasonably matches the solution [Mg]/[Si] up to [Mg]/[Si] = 1.3, although amorphous silica persisted at low ratios [39]. In another work, a comparison of solution [Mg]/[Si] and measured Mg/Si in the solid shows reasonable correspondence for low Mg/Si and early ages (24 h) and discrepancies at higher Mg/Si (i.e., >1.00) [38]. These discrepancies may be caused by the co-precipitation of silica and brucite, as discussed below. Nonetheless, the Mg/Si molar ratios of selected

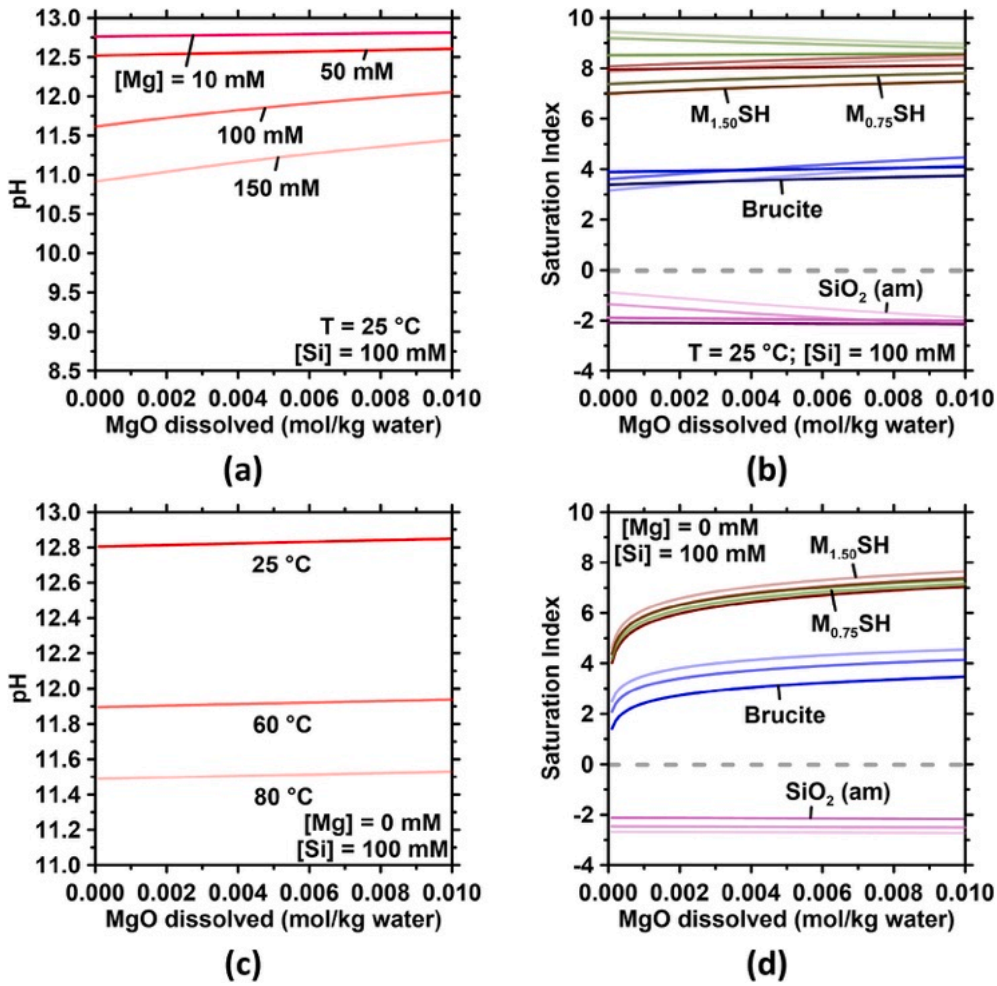

Fig. 4. Results of geochemical modeling for solutions containing 100 mM Na_2SiO_3 reacted with MgO surfaces, showing (a) pH at Mg (added as $Mg(NO)_3$) concentrations, [Mg], of 10, 50, 100, and 150 mM, (b) corresponding saturation indices with respect to brucite, amorphous silica, $M_{0.75}SH$, and $M_{1.5}SH$, for [Mg] of (*dark*) 10 mM, (*medium–dark*) 50 mM, (*medium*) 100 mM, and (*light*) 150 mM. Results of geochemical modeling for 100 mM Na_2SiO_3 reacted with MgO surfaces, showing (c) pH at 25, 60, and 80 °C, (d) corresponding saturation indices with respect to brucite, amorphous silica, $M_{0.75}SH$, and $M_{1.5}SH$, for reaction temperatures of (*dark*) 25 °C, (*medium*) 60 °C, and (*light*) 80 °C. Dashed horizontal lines indicate a saturation index of 0, corresponding to dissolution-precipitation equilibrium.

precipitated solids measured using EDS are 1.31 for [Mg]/[Si] = 1.5 and 0.53 for [Mg]/[Si] = 0.5, showing general agreement with the initial [Mg]/[Si] of the growth solution (Figs. S1 and S2, Table S5), consistent with studies that confirm the presence of MSH [38].

MSH is known to have a molecular structure similar to talc, albeit featuring disorder of the TOT structure [33,52], and to lizardite ($Mg_3(Si_2O_5)(OH)_4$), antigorite ($Mg_3(Si_2O_5)(OH)_4$), or chrysotile ($Mg_3(Si_2O_5)(OH)_4$) depending on the Mg/Si ratio of the solid [53,54]. Similar to sheet silicates such as serpentines and other clay minerals, MSH features Mg—OH bonds [38]. MSH crystallites are typically on the order of 1.2–2.4 nm in size [33,40], with interlayers that contain exchangeable cations and water molecules. The degree of interlayer hydration increases with Mg/Si [33], although other studies have noted limited interlayer water contents in MSH resembling talc [38,41]. The polymerization of silica tetrahedra in silicates such as MSH (~630–1400 cm^{-1}) can be characterized from the relative amounts of Q^0 (i.e., no oxygen sharing between silicon atoms), Q^1 (i.e., one oxygen shared between two silicon atoms), Q^2 (two shared oxygens, forming chains), and Q^3 (three shared oxygens, forming sheets) [15,55,56]. The presence of fully polymerized silica tetrahedra, Q^4, suggests the formation of amorphous SiO_2. FTIR has been used previously to characterize the silica connectivity within hydrated silicates. For instance, it has been previously shown that extended curing at high temperatures (85 °C) increases MSH crystallinity, as evidenced by the well-defined FTIR peaks that correspond to Si—O stretch and O—H stretch and bend, and the increase in Q^3/Q^2 sites together with a reduction in Q^1 sites, indicative of increased silica polymerization [38]. The peak at 3698 cm^{-1} (not distinct herein) is attributed to brucite [57], whereas 3676 cm^{-1} is attributed to O—H stretching present in MSH, and 1637 cm^{-1} arises from H—O—H bending of water confined in the interlayers or adsorbed on the surface of MSH [33,39,58]. Finally, the peak at 1350 cm^{-1} can be attributed to deprotonated (i.e., negatively charged) silanol groups ($Si—O^-$) that may form at the surfaces of amorphous silica at high pH or their complex with Mg^{2+} to form $Si—O^-—Mg^{2+}$ at MSH surfaces as observed for a calcium silicate [59]. The peaks at 835 cm^{-1} and 1340 to 1369 cm^{-1} may also be related to NO_3 symmetric and asymmetric stretching [60]; SEM-EDS data show the persistence of nitrogen in the precipitates (Figs. S1 and S2). In addition, the peak at ~620 cm^{-1} is attributable to Q^0, as in the nesosilicate, forsterite (Mg_2SiO_4) [61–64].

To understand how MSH composition influences silica tetrahedral connectivity and phase assemblage, we plotted ratios of absorbance intensities as a function of [Mg]/[Si] ratio (Fig. 3), where the species concentration is proportional to the absorbance following the Beer-Lambert Law. We used peak intensities instead of peak areas for enhanced accuracy because the presence of multiple overlapping peaks precludes accurate peak decomposition. Because the peak intensities are not calibrated for actual concentrations, they are employed to identify

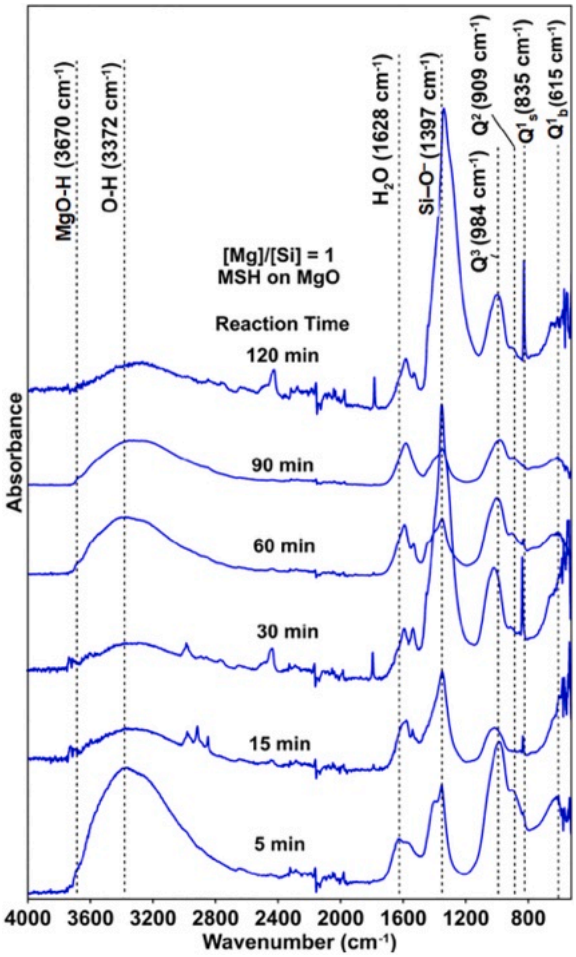

Fig. 5. Fourier-transform infrared spectra of MSH samples grown on MgO from MSH-supersaturated solutions containing [Mg] = [Si] = 100 mM ([Mg]/[Si] = 1) at 25 °C for reaction times ranging from 5 to 120 min. The wavenumbers corresponding to the species detected in each sample are labeled by dashed vertical lines.

trends across [Mg]/[Si] ratios rather than absolute concentrations of species. Other factors such as the scattering caused by particulates in the sample were not considered. The absorbances were normalized to the intensity of the H_2O peak (~1637 cm^{-1}) to isolate effects of water content on MSH structure. It has been shown for CSH that while the H_2O/Si ratio increases with Ca/Si in the solid, the H_2O/Ca ratio decreases with Ca/Si, such that the water content, which depends strongly on drying conditions, is independent of Ca/Si [65]. For MSH, the H_2O/Mg ratio is independent of Mg/Si, resulting in higher H_2O/Si at higher Mg/Si [33]. While we observed strong positive correlations between the water content and the intensities of Q^1, Q^2, and Q^3, i.e., relating to silica tetrahedral structure (Fig. 3a), we note that there is no correlation (R^2 = 0.01) between the intensity of the water peak and [Mg]/[Si].

For 0.5 < [Mg]/[Si] < 1.5, increasing Mg concentration results in decreases in the absorbances of Q^3 and Q^2 and increases in Q^1 bending (Q^1_s) and stretching (Q^1_b) vibrations (Fig. 3b). These results suggest that increasing [Mg]/[Si] (and increasing the Mg/Si molar ratio in the solid) results in depolymerization of silica tetrahedra within MSH, which agree with prior work [39]. The depolymerization of MSH is concurrent with an increase in O—H stretching in MSH with increasing [Mg]/[Si] for [Mg]/[Si] = 0.5–1.0 (Fig. 3b). Similarly, the normalized absorbance for deprotonated silanol (Si—O^-), which can be attributed to the deprotonation of amorphous silica at high pH, increases rapidly for [Mg]/[Si] = 0.5–1.0 and remains nearly constant when [Mg]/[Si] is further increased to 1.5. A decrease in pH, such as that resulting from brucite or MSH precipitation, results in a shift from undersaturation to supersaturation with respect to silica (Fig. 1c). Overall, these observations show that the precipitation of brucite or MSH *enables* the formation of silica. The co-precipitation of brucite and silica with MSH may have implications on long-term strength of MSH, possibly via mechanisms analogous to pozzolanic reactions in CSH [66,67].

It is also evident that the amounts of Q^1_s and Q^1_b increase to the same extent with increasing [Mg]/[Si], such that the absorbance ratio between Q^1_s and Q^1_b is constant (Fig. 3c). Likewise, the Q^3/Q^2 ratio is invariant with [Mg]/[Si] and is on average 1.65 ± 0.08 (where the uncertainty reflects one standard deviation). If we consider Q^3 species as representing silica sheets and Q^2 as representing defects within these sheets [39,40,68], this observation would imply that the defect density does not change significantly with changing MSH composition. Instead, significant re-organization of MSH results in its depolymerization to form silica tetrahedral pairs (Q^1).

3.2. The morphology of MSH at the nano-to-mesoscale

3.2.1. Geochemical modeling

In addition to chemical characterization of MSH shown above, we also performed time-resolved morphological characterization at the nano-to-mesoscale using AFM (**Set B**, Table 3). In general, the solutions that were reacted with either mica or MgO are initially supersaturated with respect to $M_{0.75}SH$, $M_{1.5}SH$, and brucite, and undersaturated with respect to amorphous silica (Fig. 4a, b). As discussed in Section 3.1, the rapid precipitation of MSH (at low [Mg]/[Si]) or brucite (at high [Mg]/[Si]) may enable the formation of amorphous silica by decreasing the pH. In selected experiments with MgO, the initial solutions did not contain Mg (Fig. 4c, d). Herein, the nucleation and growth of MSH rely on the dissolution of MgO, which supplies aqueous Mg^{2+} ions. On the

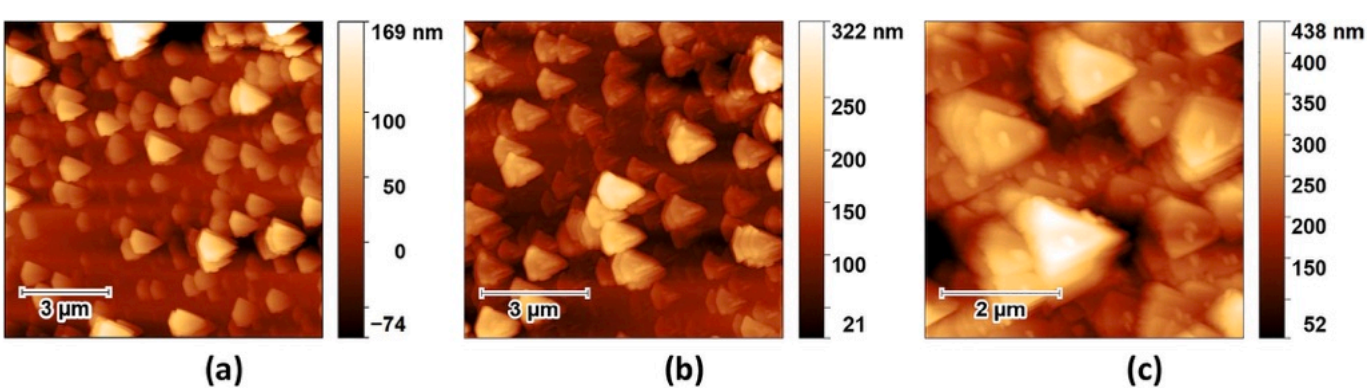

Fig. 6. Atomic force micrographs of precipitate films grown on MgO (100) after reaction with an MSH-supersaturated solution containing [Mg] = 50 mM; [Si] = 100 mM; [Mg]/[Si] = 0.5 at 25 °C for (a) 5 min, (b) 30 min, and (c) 120 min. The images are collected where thin precipitate films are evident from optical microscopy.

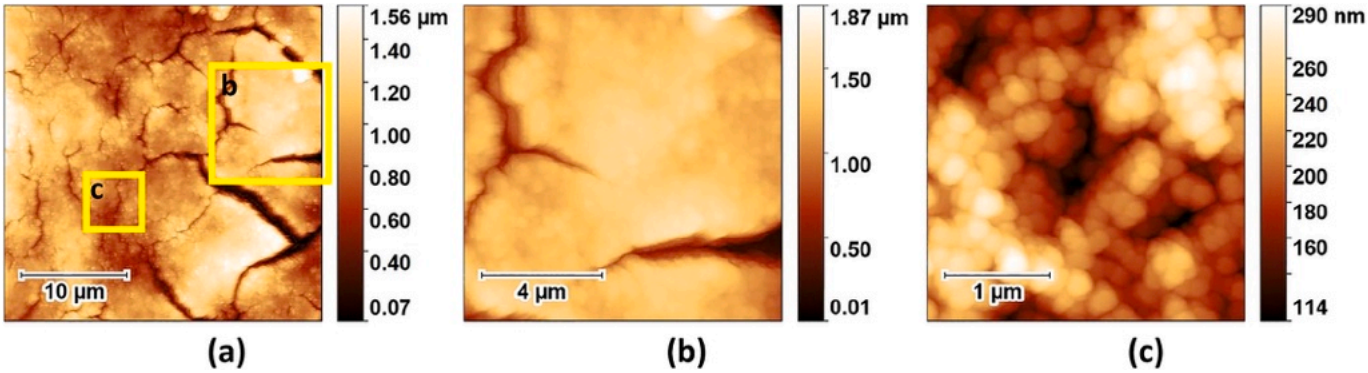

Fig. 7. Atomic force micrographs of the precipitate films grown on MgO (100) after reaction with an MSH-supersaturated solution containing [Mg] = 50 mM; [Si] = 100 mM ([Mg]/[Si] = 0.5) at 25 °C for 15 min showing (a) MSH films formed from coalescence of nanoparticles shown in detail in (b) and (c), whose relative locations are marked by yellow boxes in (a). The images are collected where thick precipitate films are evident from optical microscopy. (For interpretation of the references to color in this figure legend, the reader is referred to the web version of this article.)

contrary, MSH may directly precipitate from supersaturated solutions without the dissolution of MgO. Geochemical modeling shows that MgO dissolution initially increases both solution pH and SI with respect to brucite, $M_{0.75}SH$, and $M_{1.5}SH$ at low [Mg], and then decreases SI with respect to $M_{1.5}SH$ at high [Mg] (Fig. 4a, b). Furthermore, increasing the temperature to 60 and 80 °C reduces the pH, and for undersaturated solutions, MgO dissolution rapidly induces supersaturation with respect to Mg-containing phases (Fig. 4c, d). The simulations also reveal that at 25 °C, $M_{0.75}SH$ is the most thermodynamically favored phase, whereas $M_{1.5}SH$ is the most stable phase at 60 °C and 80 °C (Fig. 4d). The surface area of MgO in contact with the solution will affect how the saturation state evolves. During in situ experiments, only one face of the crystal is exposed to the solution, presumably resulting in lower Mg^{2+} concentration in solution compared with that during ex situ experiments, in which the entire crystal (with all its faces exposed) is immersed in the solution. Representative FTIR spectra for selected **Set B** samples show absorbance peaks characteristic of MSH production over time (Fig. 5), whereas XRD data confirm the presence of MSH on the MgO substrates (Fig. S3). The nature of our samples (thin hydrated films grown on a substrate) presents a challenge for detailed and fully quantitative analysis of chemical composition. Specifically, the thickness of MSH on MgO is on the order of a few microns that are difficult to detect using XRD because of very low signals. In addition, as shown in previous studies, MSH is poorly crystalline, and its diffraction peaks are broad, making them difficult to distinguish from the background. We propose that because of these factors, only the most intense peak at $2\theta = \sim 5°$ can be observed (note that a logarithmic scale is used on the y-axis).

3.2.2. *Atomic force microscopy observations of colloidal aggregation of MSH*

We followed the development of topography of the MgO surfaces reacted with MSH-supersaturated solutions (Table 3, Figs. 6–8). Although significant structural differences are observed in FTIR as a function of [Mg]/[Si] (Section 3.1), precipitate morphologies observed in the AFM are indistinguishable for [Mg]/[Si] = 0.5, 1.0, and 1.5 (e.g., see Figs. 7, 8, and S4). The distribution of precipitates on the MgO surface is not uniform. Particularly, for reaction durations <1 h, both thin and thick precipitate films are evident from optical microscopy. The predominant features depend on precipitate thickness. In thin areas, i.e., where the MgO surface can be easily discerned from the precipitate film, triangular precipitates are common (Fig. 6). We assign these triangular precipitates to brucite, which rapidly forms when MgO is exposed to water [69], consistent with geochemical modeling and with observations from separate AFM experiments wherein MgO is reacted with DI water in the absence of dissolved silicon (Fig. S5). Although the saturation indices are greater for MSH phases than for brucite, the persistence of brucite (for at least 2 h) indicates a strong kinetic control for brucite precipitation. There may also be differences in the local supersaturation with respect to brucite, particularly at the MgO–solution interface where much higher [Mg^{2+}] could persist [70,71].

Thicker precipitates are composed of clusters of spheroidal nanoparticles (<~100–200 nm in diameter) that form a densified film (~1.5 µm thick) over time (Figs. 7, 8). These features are reminiscent of foil-like networks in CSH [72], although CSH networks are composed of platy nanoparticles instead of globular nanoparticles as in MSH [15,73,74]. We postulate that the fundamental building blocks of MSH are smaller (on the order of 50 nm in diameter), as evidenced from AFM images collected at initially undersaturated conditions (Fig. 9a). These results support previous small-angle and wide-angle X-ray scattering (SAXS, WAXS), and scanning electron microscopy (SEM) data that reveal compactly packed polydisperse spheres that form fractal structures in MSH [73]. Interestingly, the gradual disappearance of grain boundaries indicates that the nanoparticles not only aggregated but also fused with no preferred orientations (Fig. 7b, c). Moreover, it is evident from the microcracks that arise that the coalescence of nanoparticles did not result in complete space filling (Fig. 7a, b). In general, these data reveal a complex growth mode for MSH. They suggest that rapid precipitation at high initial saturation indices (Table 3) resulted in multiple nucleation sites leading to the formation of several domains. Such colloidal aggregates can be described as either colloidal crystals or mesocrystals, depending on the presence of long-range order [75,76]. These MSH precursors are transiently stabilized, and undergo either a solid-state transition to form larger particles or dissolution-reprecipitation at grain boundaries through the occlusion of water molecules within the nanopores [77–79]. Therefore, even in the absence of additives, the abundance of highly hydrated Mg^{2+} ions may have resulted in the formation of gel-like crystallization precursors, i.e., prenucleation clusters [80], that are hygroscopic, resulting in increased cohesiveness of the primary particles as has been shown for mixed metal carbonates [77,81].

At longer reaction times, larger particles (~2 to 5 µm in diameter) form and coalesce to create another layer on top of the previously grown ("primary") film (Fig. 8). The shift toward larger (micron-sized) primary particles suggests that as dissolved ions are sequestered into the growing solid and the SI_{MSH} of the solution decreases, fewer nucleation sites develop. Furthermore, it appears that the secondary film is more continuous (Fig. 8e, f). This implies that the primary film may serve as a mediator for further growth of MSH on the MgO surface, which has been previously shown for $CaCO_3$ in the presence of organic additives [82]. Similar to the observations for the primary film, grain boundaries along micron-sized particles disappeared, perhaps through monomer-by-monomer growth or recrystallization. These observations suggest that the lower free energy of smaller particles [83] enabled the formation of a metastable primary layer on which stable MSH microparticles form.

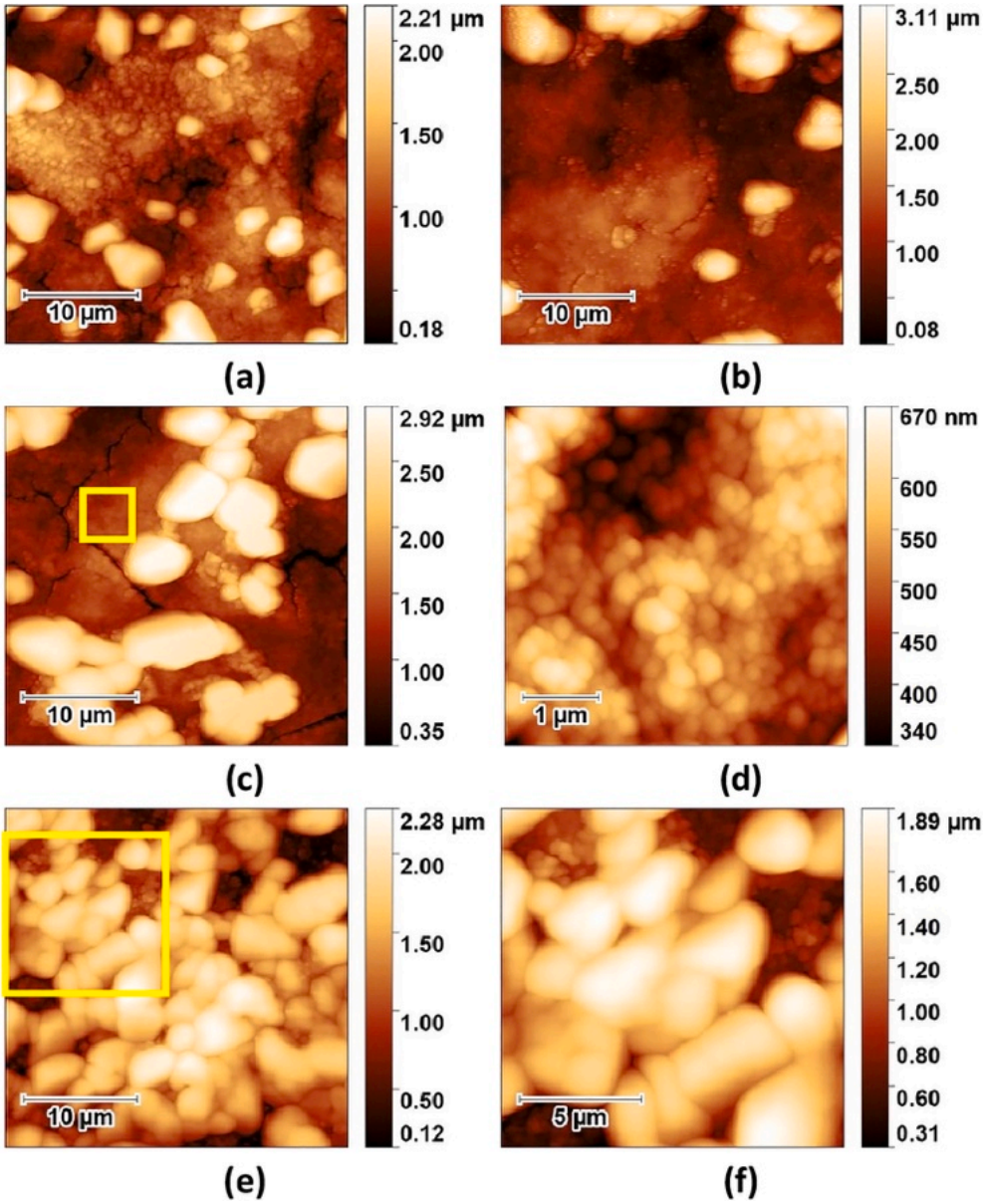

Fig. 8. Atomic force micrographs of precipitate films grown on MgO (100) after reaction with an MSH-supersaturated solution containing [Mg] = 150 mM; [Si] = 100 mM ([Mg]/[Si] = 1.5) at 25 °C for (a) 30 min, (b) 60 min, (c–d) 90 min, and (e–f) 120 min. (d) and (f) show details of areas marked by yellow boxes in (c) and (d). The images are collected where thick precipitate films are evident from optical microscopy. (For interpretation of the references to color in this figure legend, the reader is referred to the web version of this article.)

Therefore, the AFM observations demonstrate the growth of MSH layers via particle attachment, a non-classical pathway for crystallization and an indication of structural hierarchy in MSH [84]. More work is needed to determine various operative processes in both classical and non-classical mechanisms of mineral precipitation that overlap in time and space [84]. Significantly, the control of mesostructure has been demonstrated for three-dimensionally ordered CSH mesocrystals leading to excellent bending strength [85].

While the formation of brucite in thicker precipitates cannot be excluded because the growth solutions are supersaturated with respect to both MSH and brucite, we argue that the mode of growth highlighted in the AFM experiments in Figs. 7, 8, and 9 most likely pertains to MSH. AFM observations provide evidence that both brucite and MSH are present on the MgO surface, with brucite having a morphology that is consistent with its crystallographic structure (Fig. 6), and MSH featuring various morphologies that depend on the temperature and reaction time. The presence of other crystalline phases besides MSH that is consistent with peaks shown in the XRD data (Fig. S3) may correspond to the Na- and O-rich crystalline-appearing phase observed using SEM (Fig. S1). This phase has a plate-like morphology that is very distinct from that observed in the AFM images showing nanoparticle aggregation in MSH (Figs. 7, 8). Furthermore, while amorphous silica and brucite may have formed in small amounts, the following specific evidence show that MSH is the dominant phase that forms: (1) FTIR and XRD do not show significant amounts of brucite, and AFM shows that any brucite that forms occurs as triangular precipitates on the MgO surface; (2) XRD confirms the presence of MSH, but not silica; and (3) EDS shows that the Mg to Si molar ratios of precipitates grown from similar growth solutions as those used in the AFM experiments match the Mg to Si molar ratios of the initial solutions, in agreement with previous studies. These studies confirm that MSH is the dominant phase that precipitates from solutions of sodium metasilicate and magnesium nitrate, the same chemical precursors used in the present study [38]. These considerations imply that only small amounts of brucite and silica,

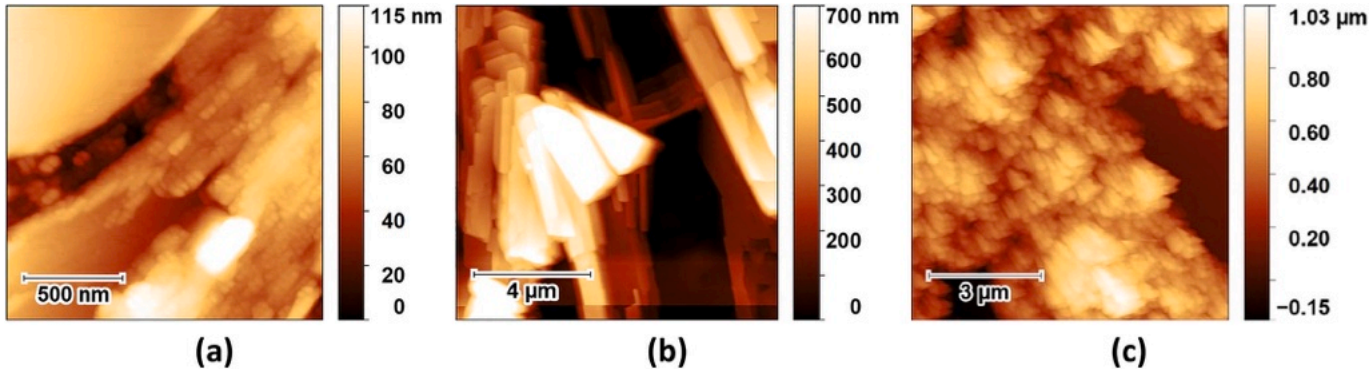

Fig. 9. Atomic force micrographs of precipitate films grown on (a-b) MgO (100) after reaction with an initially undersaturated growth solution containing [Mg] = 0 mM and [Si] = 200 mM at (a) 80 °C for 4 h, and (b) 50 °C for 5 h and then placing in the desiccator for 63 days, and (c) mica (001) after reaction with a growth solution containing [Mg] = [Si] = 200 mM at 25 °C for 1 h.

which will alter average Mg to Si molar ratios, are present. The specific contributions of brucite and silica on the AFM observations need to be further studied. This would require detailed analysis of temporally and spatially resolved changes in the morphologies and compositions of thin hydrated films deposited on single crystal substrates.

3.2.3. *Oriented growth and crystalline MSH structures*

Initially undersaturated conditions and higher temperatures (30 to 80 °C) resulted in monodisperse and oriented nanoparticles that fused to form microparticles (Fig. 9a). Oriented attachment suggests crystallographic order, wherein primary particles attach to align specific crystal faces [77]. This manner of growth resembles that operative for amorphous calcium carbonate nanoparticles grown on a calcite ($CaCO_3$) surface, in which oriented nanoparticles deposited layer-by-layer, restructured, and then fused with the crystalline substrate [86]. Triangular precipitates that are attributed to brucite (Fig. 6) were not observed, signifying that the formation of MSH, perhaps $M_{1.5}SH$ as suggested by geochemical modeling (Fig. 4d), is preferred at high temperatures. Higher temperatures and longer reaction times also resulted in the formation of prismatic, faceted, and tabular grains that are as long as a few microns, which indicates a high degree of crystallinity that is consistent with homogeneously precipitated MSH under similar conditions (Fig. 9b) [38]. Overall, these results suggest that at higher temperatures, MSH forms ordered architectures, i.e., via oriented attachment, and that these structures evolve to form crystalline MSH. Oriented attachment of nanoparticles was also observed at low temperatures (25 °C) when grown on mica (Fig. 9c). These results imply that the presence of a crystalline substrate may enhance crystallinity of MSH, e.g., via templating [87].

4. Conclusions

We systematically characterized the chemical structure of MSH formed from solutions of varying Mg/Si molar concentration ratios and investigated precipitation pathways for MSH grown on surfaces of single crystals. While this study is directed toward early precipitation (i.e., within minutes to a few days) instead of long-term (i.e., within several days to months) progression of growth, the analysis presented herein provides key insights into the effect of solution composition on growth kinetics of MSH, which ultimately controls its binding and strengthening ability. Specifically, the FTIR and geochemical modeling show that the MSH silicate framework undergoes depolymerization with increasing [Mg]/[Si]. AFM images reveal the persistence of MSH nanoparticles which fuse to form discontinuous films. These observations at the nanoscale to mesoscale reveal structural hierarchy in MSH, which can lead to nanoparticle transformation into specific microstructures that maximize macroscale performance. The unique ways by which Mg^{2+} ions may affect the hygroscopic character and cohesiveness of precursors hint at a potential for realizing alternative cements superior to CSH with respect to durability and mechanical properties. Ongoing work focuses on quantitatively characterizing the hierarchical structures in MSH. In closing, we reveal the complexity of mineral growth particularly for semi-crystalline phases such as MSH. This same complexity can be advantageous in exerting significant control over mineral precipitation and property evolution.

Declaration of competing interest

The authors declare that they have no known competing financial interests or personal relationships that could have appeared to influence the work reported in this paper.

Data availability

Data will be made available on request.

Acknowledgements

The authors acknowledge financial support provided by the National Science Foundation (NSF CAREER Award #2143159) and the U.S. Department of Energy, Office of Science, Office of Basic Energy Sciences, Geosciences Program under Contract DE-AC02-06CH11357 to UChicago Argonne, LLC as operator of Argonne National Laboratory. This work is performed at the Materials Chemistry Laboratory (MCL), the Center for Advanced Construction Materials (CACM), and the Characterization Center for Materials and Biology (CCMB) at the University of Texas at Arlington. The authors acknowledge the support that has made the operations of these laboratories possible. The contents of this paper reflect the views and opinions of the authors, who are responsible for the accuracy of the datasets presented herein, and do not reflect the views and/or polices of the agency, nor do the contents constitute a specification, standard or regulation. The U.S. Government retains for itself, and others acting on its behalf, a paid-up nonexclusive, irrevocable worldwide license in said article to reproduce, prepare derivative works, distribute copies to the public, and perform publicly and display publicly, by or on behalf of the Government.

Appendix A. Supplementary data

Supplementary data to this article can be found online at https://doi.org/10.1016/j.cemconres.2023.107367.

References

[1] P. Van den Heede, N. De Belie, Environmental impact and life cycle assessment (LCA) of traditional and 'green' concretes: literature review and theoretical

calculations, Cem. Concr. Compos. 34 (2012) 431–442, https://doi.org/10.1016/j.cemconcomp.2012.01.004.
[2] R.J. Flatt, N. Roussel, C.R. Cheeseman, Concrete: an eco material that needs to be improved, J. Eur. Ceram. Soc. 32 (2012) 2787–2798, https://doi.org/10.1016/j.jeurceramsoc.2011.11.012.
[3] E. Gartner, H. Hirao, A review of alternative approaches to the reduction of CO_2 emissions associated with the manufacture of the binder phase in concrete, Cem. Concr. Res. 78 (2015) 126–142, https://doi.org/10.1016/j.cemconres.2015.04.012.
[4] M. Fischedick, J. Roy, A. Abdel-Aziz, A. Acquaye, J.M. Allwood, J.-P. Ceron, Y. Geng, H. Kheshgi, A. Lanza, D. Perczyk, L. Price, E. Santalla, C. Sheinbaum, K. Tanaka, Industry, in: Clim. Change 2014 Mitig. Clim. Change Contrib. Work. Group III Fifth Assess. Rep. Intergov. Panel Clim. Change, Cambridge University Press, Cambridge, United Kingdom and New York, NY, USA, 2014.
[5] U. Dewald, M. Achternbosch, Why more sustainable cements failed so far? Disruptive innovations and their barriers in a basic industry, Environ. Innov. Soc. Transit. 19 (2016) 15–30, https://doi.org/10.1016/j.eist.2015.10.001.
[6] S.A. Walling, J.L. Provis, Magnesia-based cements: a journey of 150 years, and cements for the future? Chem. Rev. 116 (2016) 4170–4204, https://doi.org/10.1021/acs.chemrev.5b00463.
[7] J. Rieger, M. Kellermeier, L. Nicoleau, Formation of nanoparticles and nanostructures—an industrial perspective on $CaCO_3$, cement, and polymers, Angew. Chem. Int. Ed. 53 (2014) 12380–12396, https://doi.org/10.1002/anie.201402890.
[8] A. Nonat, The structure and stoichiometry of C-S-H, Cem. Concr. Res. 34 (2004) 1521–1528, https://doi.org/10.1016/j.cemconres.2004.04.035.
[9] H.F.W. Taylor, Proposed structure for calcium silicate hydrate gel, J. Am. Ceram. Soc. 69 (1986) 464–467, https://doi.org/10.1111/j.1151-2916.1986.tb07446.x.
[10] X. Cong, R.J. Kirkpatrick, ^{29}Si MAS NMR study of the structure of calcium silicate hydrate, Adv. Cem. Bas. Mat. 3 (1996) 144–156, https://doi.org/10.1016/S1065-7355(96)90046-2.
[11] I.G. Richardson, Tobermorite/jennite- and tobermorite/calcium hydroxide-based models for the structure of C-S-H: applicability to hardened pastes of tricalcium silicate, β-dicalcium silicate, Portland cement, and blends of Portland cement with blast-furnace slag, metakaolin, or silica fume, Cem. Concr. Res. 34 (2004) 1733–1777, https://doi.org/10.1016/j.cemconres.2004.05.034.
[12] J.J. Chen, J.J. Thomas, H.F.W. Taylor, H.M. Jennings, Solubility and structure of calcium silicate hydrate, Cem. Concr. Res. 34 (2004) 1499–1519, https://doi.org/10.1016/j.cemconres.2004.04.034.
[13] M.C. Braney, A. Haworth, N.L. Jefferies, A.C. Smith, A study of the effects of an alkaline plume from a cementitious repository on geological materials, J. Contam. Hydrol. 13 (1993) 379–402, https://doi.org/10.1016/0169-7722(93)90072-Z.
[14] A. Duguid, J. Kirksey, D. Riestenberg, G. Koperna, C. Holley, M. Loizzo, R. Locke, CO_2 Well Construction: Lessons Learned from United States Department of Energy Sponsored Projects, Southern States Energy Board, Peachtree Corners, GA (United States), 2018.
[15] M.R. Marsiske, C. Debus, F. Di Lorenzo, E. Bernard, S.V. Churakov, C. Ruiz-Agudo, Immobilization of (aqueous) cations in low pH M-S-H cement, Appl. Sci. 11 (2021) 2968, https://doi.org/10.3390/app11072968.
[16] T. Zhang, C.R. Cheeseman, L.J. Vandeperre, Development of low pH cement systems forming magnesium silicate hydrate (M-S-H), Cem. Concr. Res. 41 (2011) 439–442, https://doi.org/10.1016/j.cemconres.2011.01.016.
[17] E. Bernard, B. Lothenbach, C. Cau-Dit-Coumes, I. Pochard, D. Rentsch, Aluminum incorporation into magnesium silicate hydrate (M-S-H), Cem. Concr. Res. 128 (2020), 105931, https://doi.org/10.1016/j.cemconres.2019.105931.
[18] T. Zhang, C. Cheeseman, L.J. Vandeperre, Characterisation of corrosion of nuclear metal wastes encapsulated in magnesium silicate hydrate (MSH) cement, in: K. Fox, Y. Katoh, H.-T. Lin, I. Belharouak, M. Halbig, S. Mathur (Eds.), Ceram. Eng. Sci. Proc., John Wiley & Sons, Inc., Hoboken, NJ, USA, 2012, pp. 159–167, https://doi.org/10.1002/9781118217535.ch12.
[19] N.B. Milestone, Reactions in cement encapsulated nuclear wastes: need for toolbox of different cement types, Adv. Appl. Ceram. 105 (2006) 13–20, https://doi.org/10.1179/174367606X81678.
[20] Longfei Lin, The Key Parameters Influencing the Reactivity of Magnesium Silicate Based Catalysts: Application to Transesterification in Liquid Phase, NNT: 2017PA066313, Université Pierre et Marie Curie, 2017. https://tel.archives-ouvertes.fr/tel-01719278/document.
[21] United States Geological Survey, Magnesium Resources of the United States: A Geologic Summary and Annotated Bibliography to 1953. https://pubs.usgs.gov/bul/1019e/report.pdf, 1957.
[22] S.L. Qi, A.C. Harris, Geochemical Database for the Brackish Groundwater Assessment of the United States: U.S. Geological Survey data release, 2017, https://doi.org/10.5066/F72F7KK1.
[23] E. Jones, M. Qadir, M.T.H. van Vliet, V. Smakhtin, S. Kang, The state of desalination and brine production: a global outlook, Sci. Total Environ. 657 (2019) 1343–1356, https://doi.org/10.1016/j.scitotenv.2018.12.076.
[24] Produced Waters - Homepage, USGS: Energy Resources Program, n.d. https://energy.usgs.gov/EnvironmentalAspects/EnvironmentalAspectsofEnergyProductionandUse/ProducedWaters.aspx#3822110-overview. (Accessed 4 April 2018).
[25] E. Nduagu, I. Romão, J. Fagerlund, R. Zevenhoven, Performance assessment of producing $Mg(OH)_2$ for CO_2 mineral sequestration, Appl. Energy 106 (2013) 116–126, https://doi.org/10.1016/j.apenergy.2013.01.049.
[26] L. de Ruiter, A.E. Gunnæs, D.K. Dysthe, H. Austrheim, Quartz dissolution associated with magnesium silicate hydrate cement precipitation, Solid Earth Discuss. (2020) 1–25, https://doi.org/10.5194/se-2020-34.
[27] V. Chavagnac, C. Monnin, G. Ceuleneer, C. Boulart, G. Hoareau, Characterization of hyperalkaline fluids produced by low-temperature serpentinization of mantle peridotites in the Oman and Ligurian ophiolites, Geochem. Geophys. Geosyst. 14 (2013) 2496–2522, https://doi.org/10.1002/ggge.20147.
[28] L. de Ruiter, H. Austrheim, Formation of magnesium silicate hydrate cement in nature, J. Geol. Soc. London 175 (2018) 308–320, https://doi.org/10.1144/jgs2017-089.
[29] W.F. Cole, A crystalline hydrated magnesium silicate formed in the breakdown of a concrete sea-wall, Nature 171 (1953) 354–355, https://doi.org/10.1038/171354a0.
[30] G. Bai, H.-B. Yi, H.-J. Li, J.-J. Xu, Hydration characteristics of Ca^{2+} and Mg^{2+}: a density functional theory, polarized continuum model and molecular dynamics investigation, Mol. Phys. 111 (2013) 553–568, https://doi.org/10.1080/00268976.2012.737035.
[31] D. Jiao, C. King, A. Grossfield, T.A. Darden, P. Ren, Simulation of Ca^{2+} and Mg^{2+} solvation using polarizable atomic multipole potential, J. Phys. Chem. B 110 (2006) 18553–18559, https://doi.org/10.1021/jp062230r.
[32] C. Labbez, B. Jönsson, I. Pochard, A. Nonat, B. Cabane, Surface charge density and electrokinetic potential of highly charged minerals: experiments and Monte Carlo simulations on calcium silicate hydrate, J. Phys. Chem. B 110 (2006) 9219–9230, https://doi.org/10.1021/jp057096+.
[33] E. Bernard, B. Lothenbach, C. Chlique, M. Wyrzykowski, A. Dauzères, I. Pochard, C. Cau-Dit-Coumes, Characterization of magnesium silicate hydrate (M-S-H), Cem. Concr. Res. 116 (2019) 309–330, https://doi.org/10.1016/j.cemconres.2018.09.007.
[34] H. Viallis-Terrisse, A. Nonat, J.-C. Petit, Zeta-potential study of calcium silicate hydrates interacting with alkaline cations, J. Colloid Interface Sci. 244 (2001) 58–65, https://doi.org/10.1006/jcis.2001.7897.
[35] N.J. Tosca, A.L. Masterson, Chemical controls on incipient Mg-silicate crystallization at 25 °C: implications for early and late diagenesis, Clay Miner. 49 (2014) 165–194, https://doi.org/10.1180/claymin.2014.049.2.03.
[36] G.L. Kalousek, D. Mui, Studies on formation and recrystallization of intermediate reaction products in the system magnesia-silica-water, J. Am. Ceram. Soc. 37 (1954) 38–42, https://doi.org/10.1111/j.1151-2916.1954.tb14001.x.
[37] J.C.-S. Yang, The system magnesia-silica-water below 300 °C.: I, low-temperature phases from 100° to 300 °C. And their properties, J. Am. Ceram. Soc. 43 (1960) 542–549, https://doi.org/10.1111/j.1151-2916.1960.tb13610.x.
[38] D.R.M. Brew, F.P. Glasser, Synthesis and characterisation of magnesium silicate hydrate gels, Cem. Concr. Res. 35 (2005) 85–98, https://doi.org/10.1016/j.cemconres.2004.06.022.
[39] D. Nied, K. Enemark-Rasmussen, E. L'Hopital, J. Skibsted, B. Lothenbach, Properties of magnesium silicate hydrates (M-S-H), Cem. Concr. Res. 79 (2016) 323–332, https://doi.org/10.1016/j.cemconres.2015.10.003.
[40] C. Roosz, S. Grangeon, P. Blanc, V. Montouillout, B. Lothenbach, P. Henocq, E. Giffaut, P. Vieillard, S. Gaboreau, Crystal structure of magnesium silicate hydrates (M-S-H): the relation with 2:1 Mg–Si phyllosilicates, Cem. Concr. Res. 73 (2015) 228–237, https://doi.org/10.1016/j.cemconres.2015.03.014.
[41] C. Roosz, P. Vieillard, P. Blanc, S. Gaboreau, H. Gailhanou, D. Braithwaite, V. Montouillout, R. Denoyel, P. Henocq, B. Madé, Thermodynamic properties of C-S-H, C-A-S-H and M-S-H phases: results from direct measurements and predictive modelling, Appl. Geochem. 92 (2018) 140–156, https://doi.org/10.1016/j.apgeochem.2018.03.004.
[42] M. Vespa, B. Lothenbach, R. Dähn, T. Huthwelker, E. Wieland, Characterisation of magnesium silicate hydrate phases (M-S-H): a combined approach using synchrotron-based absorption-spectroscopy and ab initio calculations, Cem. Concr. Res. 109 (2018) 175–183, https://doi.org/10.1016/j.cemconres.2018.03.011.
[43] E. Bernard, B. Lothenbach, C. Cau-Dit-Coumes, C. Chlique, A. Dauzères, I. Pochard, Magnesium and calcium silicate hydrates, part I: investigation of the possible magnesium incorporation in calcium silicate hydrate (C-S-H) and of the calcium in magnesium silicate hydrate (M-S-H), Appl. Geochem. 89 (2018) 229–242, https://doi.org/10.1016/j.apgeochem.2017.12.005.
[44] D.L. Parkhurst, C.A.J. Appelo, Description of input and examples for PHREEQC version 3—a computer program for speciation, batch-reaction, one-dimensional transport, and inverse geochemical calculations, US Geol. Surv. Tech. Methods Book. 6 (2013) 497.
[45] B. Lothenbach, D.A. Kulik, T. Matschei, M. Balonis, L. Baquerizo, B. Dilnesa, G. D. Miron, R.J. Myers, Cemdata18: a chemical thermodynamic database for hydrated Portland cements and alkali-activated materials, Cem. Concr. Res. 115 (2019) 472–506, https://doi.org/10.1016/j.cemconres.2018.04.018.
[46] S. Sinha Ray, Structure and Morphology Characterization Techniques, in: Clay-Contain. Polym. Nanocomposites, Elsevier, 2013, pp. 39–66, https://doi.org/10.1016/B978-0-444-59437-2.00003-X.
[47] D. Di Tommaso, N.H. de Leeuw, Structure and dynamics of the hydrated magnesium ion and of the solvated magnesium carbonates: insights from first principles simulations, Phys. Chem. Chem. Phys. 12 (2010) 894–901, https://doi.org/10.1039/B915329B.
[48] C.P. Morrow, J.D. Kubicki, K.T. Mueller, D.R. Cole, Description of Mg^{2+} release from forsterite using ab initio methods, J. Phys. Chem. C 114 (2010) 5417–5428, https://doi.org/10.1021/jp9057719.
[49] W.H. Casey, H.R. Westrich, Control of dissolution rates of orthosilicate minerals by divalent metal–oxygen bonds, Nature 355 (1992) 157–159, https://doi.org/10.1038/355157a0.
[50] M. Peschke, A.T. Blades, P. Kebarle, Hydration energies and entropies for Mg^{2+}, Ca^{2+}, Sr^{2+}, and Ba^{2+} from gas-phase ion−water molecule equilibria determinations, J. Phys. Chem. A 102 (1998) 9978–9985, https://doi.org/10.1021/jp9821127.

[51] T. Dudev, J.A. Cowan, C. Lim, Competitive binding in magnesium coordination chemistry: water versus ligands of biological interest, J. Am. Chem. Soc. 121 (1999) 7665–7673, https://doi.org/10.1021/ja984470t.
[52] M. Tonelli, F. Martini, L. Calucci, E. Fratini, M. Geppi, F. Ridi, S. Borsacchi, P. Baglioni, Structural characterization of magnesium silicate hydrate: towards the design of eco-sustainable cements, Dalton Trans. 45 (2016) 3294–3304, https://doi.org/10.1039/C5DT03545G.
[53] A. Pedone, F. Palazzetti, V. Barone, Models of aged magnesium–silicate–hydrate cements based on the Lizardite and talc crystals: a periodic DFT-GIPAW investigation, J. Phys. Chem. C 121 (2017) 7319–7330, https://doi.org/10.1021/acs.jpcc.7b00708.
[54] Y. Zhang, M. Nath, J. Wang, Y. Li, S. Zhang, T. Zhu, Z. Xue, J. Chen, Temperature-dependent rehydration of magnesium silicate hydrate (M-S-H): development of no-cement binder through MD/DFT validation, Ceram. Int. 48 (2022) 7063–7070, https://doi.org/10.1016/j.ceramint.2021.11.265.
[55] B. Lothenbach, D. Nied, E. L'Hôpital, G. Achiedo, A. Dauzères, Magnesium and calcium silicate hydrates, Cem. Concr. Res. 77 (2015) 60–68, https://doi.org/10.1016/j.cemconres.2015.06.007.
[56] E. Bernard, B. Lothenbach, D. Rentsch, I. Pochard, A. Dauzères, Formation of magnesium silicate hydrates (M-S-H), Phys. Chem. Earth Parts ABC. 99 (2017) 142–157, https://doi.org/10.1016/j.pce.2017.02.005.
[57] R.L. Frost, J.T. Kloprogge, Infrared emission spectroscopic study of brucite, Spectrochim. Acta. A. Mol. Biomol. Spectrosc. 55 (1999) 2195–2205, https://doi.org/10.1016/S1386-1425(99)00016-5.
[58] T. Zhang, J. Zou, B. Wang, Z. Wu, Y. Jia, C. Cheeseman, Characterization of magnesium silicate hydrate (MSH) gel formed by reacting MgO and silica fume, Materials 11 (2018) 909, https://doi.org/10.3390/ma11060909.
[59] R. Ellerbrock, M. Stein, J. Schaller, Comparing amorphous silica, short-range-ordered silicates and silicic acid species by FTIR, Sci. Rep. 12 (2022) 11708, https://doi.org/10.1038/s41598-022-15882-4.
[60] M. Trivedi, A. Branton, D. Trivedi, G. Nayak, K. Bairwa, S. Jana, Spectroscopic characterization of disodium hydrogen orthophosphate and sodium nitrate after biofield treatment, Chromatogr. Sep. Tech. 5 (2015).
[61] The RRUFF Project, Forsterite R050117 - RRUFF Database: Raman, X-ray, Infrared, and Chemistry, n.d. https://rruff.info/Forsterite/R050117. (Accessed 9 January 2023).
[62] M.A. Naghiu, M. Gorea, E. Mutch, F. Kristaly, M. Tomoaia-Cotisel, Forsterite nanopowder: structural characterization and biocompatibility evaluation, J. Mater. Sci. Technol. 29 (2013) 628–632, https://doi.org/10.1016/j.jmst.2013.04.007.
[63] A.M. Nojehdehi, F. Moghaddam, M.T. Hamedani, Mechanical properties of glass ionomer cement incorporating forsterite nanoparticles synthesized by the sol-gel method, J. Sol-Gel Sci. Technol. (2022), https://doi.org/10.1007/s10971-022-05792-2.
[64] B. Lafuente, R.T. Downs, H. Yang, N. Stone, The power of databases: The RRUFF project, in: Highlights Mineral. Crystallogr., De Gruyter (O), 2015, pp. 1–30.
[65] E. L'Hôpital, B. Lothenbach, D.A. Kulik, K. Scrivener, Influence of calcium to silica ratio on aluminium uptake in calcium silicate hydrate, Cem. Concr. Res. 85 (2016) 111–121, https://doi.org/10.1016/j.cemconres.2016.01.014.
[66] H.M. Tran, A. Scott, Strength and workability of magnesium silicate hydrate binder systems, Construct. Build Mater. 131 (2017) 526–535, https://doi.org/10.1016/j.conbuildmat.2016.11.109.
[67] C. Sonat, C. Unluer, Development of magnesium-silicate-hydrate (M-S-H) cement with rice husk ash, J. Clean. Prod. 211 (2019) 787–803, https://doi.org/10.1016/j.jclepro.2018.11.246.
[68] E. Bernard, Magnesium silicate hydrate (M-S-H) characterization: temperature, calcium, aluminium and alkali, phdthesis, Université Bourgogne Franche-Comté, 2017.
[69] C. Unluer, A. Al-Tabbaa, The role of brucite, ground granulated blastfurnace slag, and magnesium silicates in the carbonation and performance of MgO cements, Construct. Build Mater. 94 (2015) 629–643, https://doi.org/10.1016/j.conbuildmat.2015.07.105.
[70] J.W. Morse, R.S. Arvidson, The dissolution kinetics of major sedimentary carbonate minerals, Earth Sci. Rev. 58 (2002) 51–84, https://doi.org/10.1016/S0012-8252(01)00083-6.
[71] W.M. Murphy, E.H. Oelkers, P.C. Lichtner, Surface reaction versus diffusion control of mineral dissolution and growth rates in geochemical processes, Kinet. Geochem. 78 (1989) 357–380, https://doi.org/10.1016/0009-2541(89)90069-7.
[72] F. Basquiroto de Souza, E. Shamsaei, S. Chen, K. Sagoe-Crentsil, W. Duan, Controlled growth and ordering of poorly-crystalline calcium-silicate-hydrate nanosheets, Commun. Mater. 2 (2021) 1–11, https://doi.org/10.1038/s43246-021-00191-6.
[73] W.-S. Chiang, G. Ferraro, E. Fratini, F. Ridi, Y.-Q. Yeh, U.-S. Jeng, S.-H. Chen, P. Baglioni, Multiscale structure of calcium- and magnesium-silicate-hydrate gels, J. Mater. Chem. A 2 (2014) 12991–12998, https://doi.org/10.1039/C4TA02479F.
[74] J. Plank, M. Schönlein, V. Kanchanason, Study on the early crystallization of calcium silicate hydrate (C-S-H) in the presence of polycarboxylate superplasticizers, J. Organomet. Chem. 869 (2018) 227–232, https://doi.org/10.1016/j.jorganchem.2018.02.005.
[75] E.V. Sturm, H. Cölfen, Mesocrystals: structural and morphogenetic aspects, Chem. Soc. Rev. 45 (2016) 5821–5833, https://doi.org/10.1039/C6CS00208K.
[76] H. Cölfen, M. Antonietti, Mesocrystals: inorganic superstructures made by highly parallel crystallization and controlled alignment, Angew. Chem. Int. Ed. Engl. 44 (2005) 5576–5591, https://doi.org/10.1002/anie.200500496.
[77] M. Jehannin, A. Rao, H. Cölfen, New horizons of nonclassical crystallization, J. Am. Chem. Soc. 141 (2019) 10120–10136, https://doi.org/10.1021/jacs.9b01883.
[78] A.L. Goodwin, F.M. Michel, B.L. Phillips, D.A. Keen, M.T. Dove, R.J. Reeder, Nanoporous structure and medium-range order in synthetic amorphous calcium carbonate, Chem. Mater. 22 (2010) 3197–3205, https://doi.org/10.1021/cm100294d.
[79] A. Putnis, Mineral replacement reactions, Rev. Mineral. Geochem. 70 (2009) 87–124, https://doi.org/10.2138/rmg.2009.70.3.
[80] D. Gebauer, M. Kellermeier, J.D. Gale, L. Bergström, H. Cölfen, Pre-nucleation clusters as solute precursors in crystallisation, Chem. Soc. Rev. 43 (2014) 2348–2371, https://doi.org/10.1039/C3CS60451A.
[81] Y.-C. Huang, M.B. Gindele, J. Knaus, A. Rao, D. Gebauer, On mechanisms of mesocrystal formation: magnesium ions and water environments regulate the crystallization of amorphous minerals, CrystEngComm 20 (2018) 4395–4405, https://doi.org/10.1039/C8CE00241J.
[82] L.A. Gower, D.A. Tirrell, Calcium carbonate films and helices grown in solutions of poly(aspartate), J. Cryst. Growth 191 (1998) 153–160, https://doi.org/10.1016/S0022-0248(98)00002-5.
[83] A. Navrotsky, Energetic clues to pathways to biomineralization: precursors, clusters, and nanoparticles, Proc. Natl. Acad. Sci. U. S. A. 101 (2004) 12096–12101, https://doi.org/10.1073/pnas.0404778101.
[84] J.J. De Yoreo, P.U.P.A. Gilbert, N.A.J.M. Sommerdijk, R.L. Penn, S. Whitelam, D. Joester, H. Zhang, J.D. Rimer, A. Navrotsky, J.F. Banfield, A.F. Wallace, F. M. Michel, F.C. Meldrum, H. Cölfen, P.M. Dove, Crystallization by particle attachment in synthetic, biogenic, and geologic environments, Science 349 (2015) aaa6760, https://doi.org/10.1126/science.aaa6760.
[85] A. Picker, L. Nicoleau, Z. Burghard, J. Bill, I. Zlotnikov, C. Labbez, A. Nonat, H. Cölfen, Mesocrystalline calcium silicate hydrate: a bioinspired route toward elastic concrete materials, Sci. Adv. 3 (2017), e1701216, https://doi.org/10.1126/sciadv.1701216.
[86] C. Rodriguez-Navarro, A. Burgos Cara, K. Elert, C.V. Putnis, E. Ruiz-Agudo, Direct nanoscale imaging reveals the growth of calcite crystals via amorphous nanoparticles, Cryst. Growth Des. 16 (2016) 1850–1860, https://doi.org/10.1021/acs.cgd.5b01180.
[87] F.C. Meldrum, H. Cölfen, Controlling mineral morphologies and structures in biological and synthetic systems, Chem. Rev. 108 (2008) 4332–4432, https://doi.org/10.1021/cr8002856.